nature metabolism

Supplementary information

https://doi.org/10.1038/s42255-026-01538-4

Hyperglycosylation is a metabolic driver of Alzheimer's disease

In the format provided by the authors and unedited

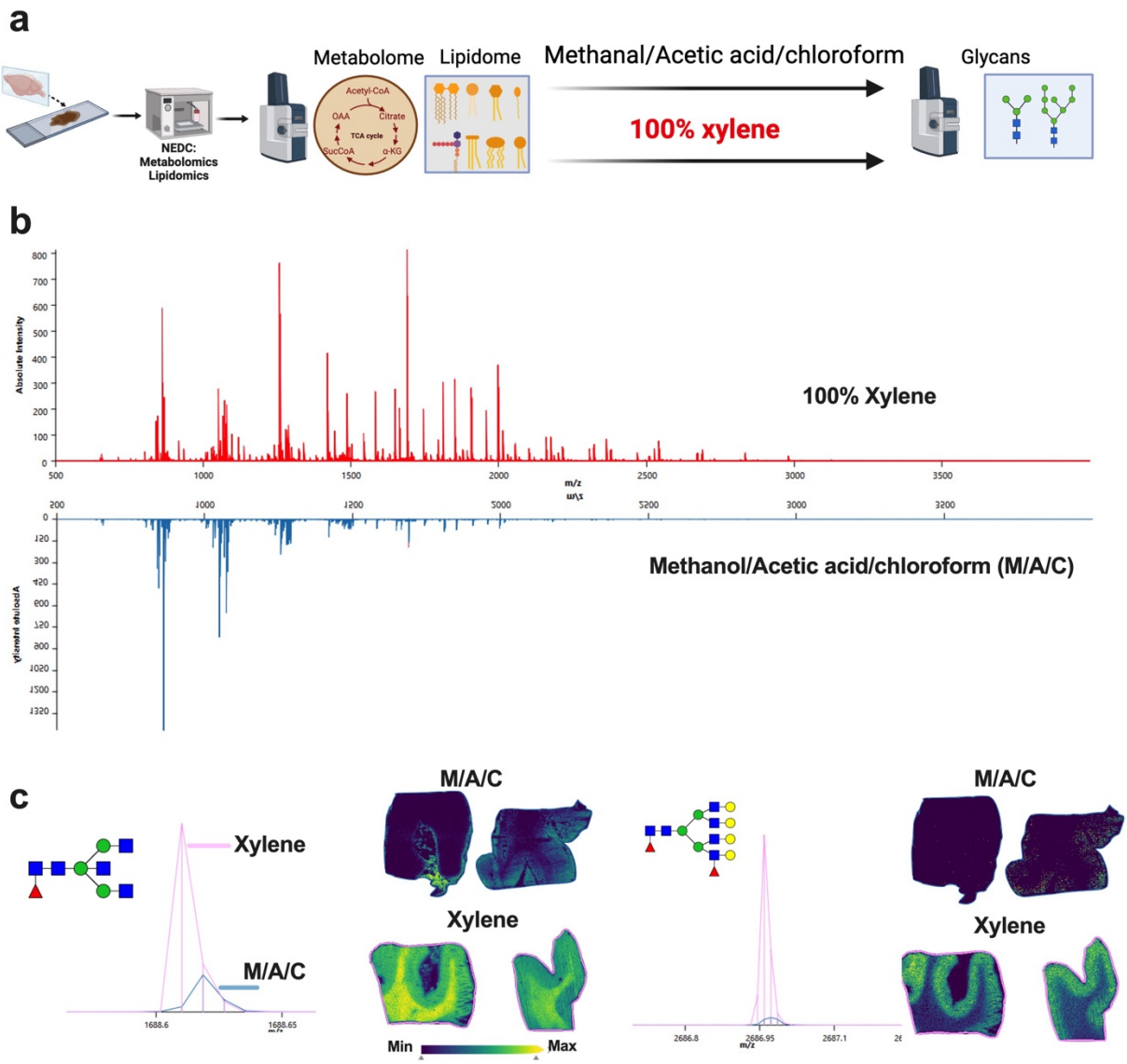

Supplementary Fig. 1 | Xylene tissue clearing preserves metabolite and lipid signals and improves glycan detection compared to Methanol/acetic acid/chloroform (M/A/C). a, Workflow schematic comparing the use of 100% xylene versus M/A/C as clearing agents in serial multimodal imaging of metabolome, lipidome, and glycome on fresh frozen brain tissue. **b**, Representative MALDI mass spectra comparing glycan signal profiles obtained from xylene-cleared (top, red) and M/A/C-cleared (bottom, blue) tissue. Xylene treatment results in reduced background and enhanced signal-to-noise ratio for glycan detection. **c**, Extracted ion chromatograms and spatial glycomics images of representative glycan species demonstrate increased detection sensitivity and spatial resolution using xylene clearing compared to M/A/C.

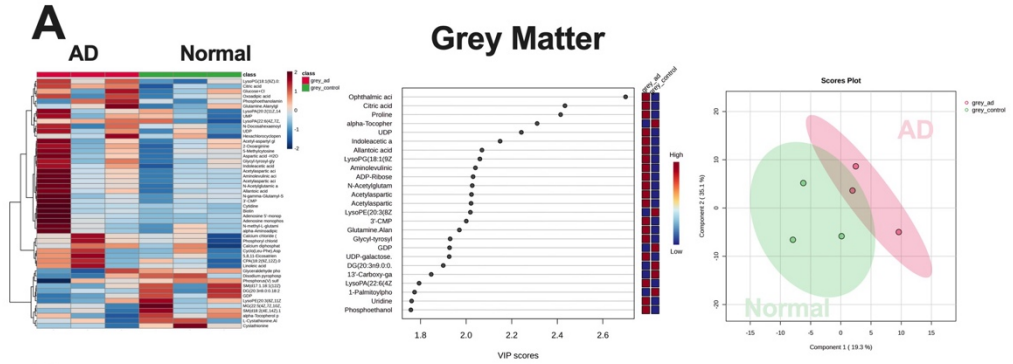
A
AD
Normal
Grey Matter
Ophthalmic aci
Citric acid
Proline
alpha-Tocopher
UDP
Indoleacetic a
Allantoic acid
LysoPG(18:1(9Z
Aminolevulinic
ADP-Ribose
N-Acetylglutam
Acetylaspartic
Acetylaspartic
LysoPE(20:3(8Z
3'-CMP
Glutamine.Alan
Glycyl-tyrosyl
GDP
UDP-galactose.
13'-Carboxy-ga
LysoPA(22:6(4Z
1-Palmitoylpho
Uridine
Phosphoethanol
VIP scores
Scores Plot
grey_ad
grey_control
AD
Normal
Component 1 (19.3 %)
Component 2 (35.1 %)

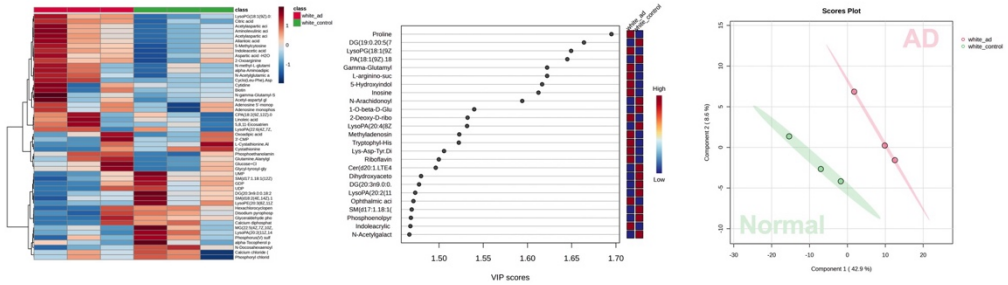
B
AD
Normal
White Matter
Proline
DG(19:0,20:5(7
LysoPG(18:1(9Z
PA(18:1(9Z).18
Gamma-Glutamyl
L-arginino-suc
5-Hydroxyindol
Inosine
N-Arachidonoyl
1-O-beta-D-Glu
2-Deoxy-D-ribo
LysoPA(20:4(8Z
Methyladenosin
Tryptophyl-His
Lys-Asp-Tyr.Di
Riboflavin
Cer(d20:1,TE4
Dihydroxyacete
DG(20:3n9.0.0.
LysoPA(20:2(11
Ophthalmic aci
SM(d17:1,18:1(
Phosphoenolpyr
Indoleacrylic
N-Acetyllactos
VIP scores
Scores Plot
white_ad
white_control
AD
Normal
Component 1 (42.9 %)
Component 2 (8.6 %)

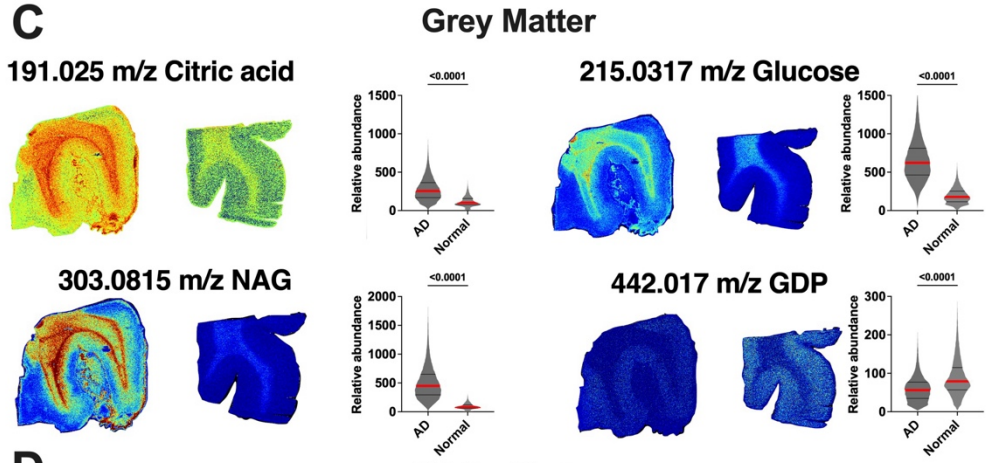
C
Grey Matter
191.025 m/z Citric acid
215.0317 m/z Glucose
303.0815 m/z NAG
442.017 m/z GDP
Relative abundance
<0.0001
AD
Normal

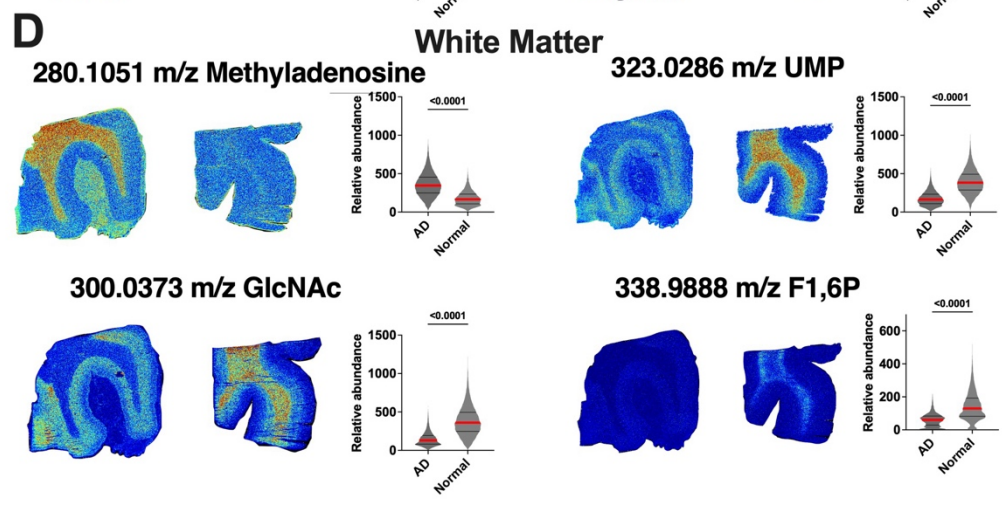
D
White Matter
280.1051 m/z Methyladenosine
323.0286 m/z UMP
300.0373 m/z GlcNAc
338.9888 m/z F1,6P
Relative abundance
<0.0001
AD
Normal

Supplementary Fig. 2 | Spatial metabolomics reveals differential metabolite abundance in grey and white matter of AD brains. a, Heatmap, VIP plot, and PCA analysis of metabolites in grey matter from Alzheimer's disease (AD) and control brains. Key altered metabolites include citric acid, glucose, and UDP-sugar intermediates. **b**, Heatmap, VIP plot, and PCA analysis for white matter metabolites. Differences in nucleotide sugars and energy metabolites distinguish AD from normal controls. **c**, Spatial metabolomics maps and violin plots of representative metabolites in grey matter, including citric acid (191.025 m/z), glucose (215.0317 m/z), N-acetylglucosamine (NAG, 303.0815 m/z), and GDP (442.017 m/z), all showing significantly decreased abundance in AD. **d**, Spatial metabolomics visualization and quantification in white matter for methyladenosine (280.1051 m/z), UMP (323.0286 m/z), GlcNAc (300.0373 m/z), and fructose-1,6-bisphosphate (338.9888 m/z). Statistical significance assessed via two-tailed t-tests; exact P-values indicated. (N>2000 pixels per 3 biological replicates).

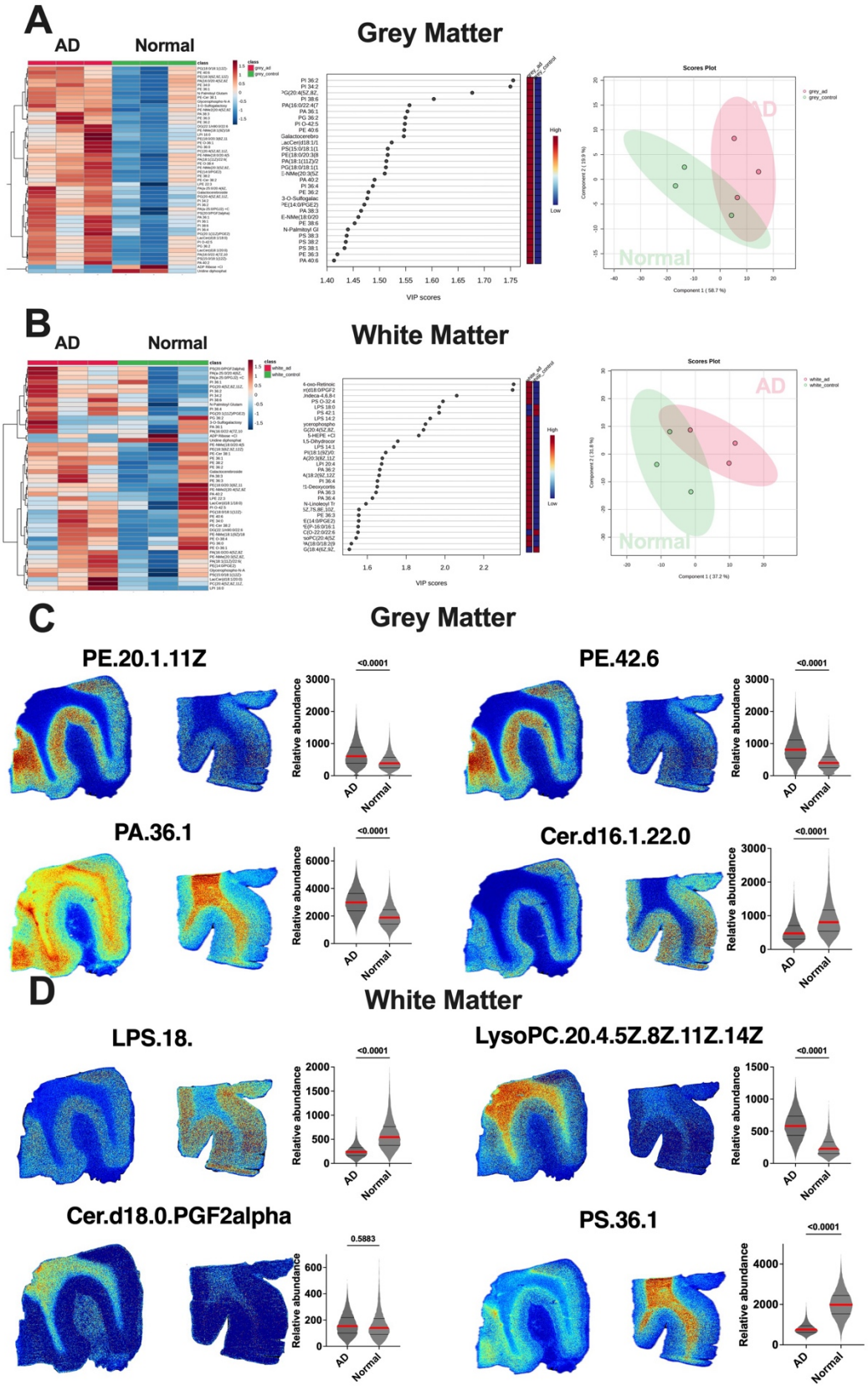
A
AD
Normal
Grey Matter
VIP scores
Scores Plot
Component 1 (58.7 %)
B
White Matter
VIP scores
Component 1 (37.2 %)
C
Grey Matter
PE.20.1.11Z
PE.42.6
PA.36.1
Cer.d16.1.22.0
D
White Matter
LPS.18.
LysoPC.20.4.5Z.8Z.11Z.14Z
Cer.d18.0.PGF2alpha
PS.36.1
Relative abundance
<0.0001
0.5883

Supplementary Fig. 3 | Spatial lipidomics reveals region-specific lipid alterations in Alzheimer's disease brains. a, Heatmap, VIP score ranking, and PCA of lipid species in grey matter comparing AD and control brains, showing distinct segregation and increased levels of phosphatidylinositol (PI), phosphatidylethanolamine (PE), and phosphatidylserine (PS) subclasses in AD. **b**, Corresponding analyses in white matter reveal elevation of cardiolipin (CL), phosphatidylglycerol (PG), and ether-linked phospholipids in AD compared to controls. **c**, Spatial maps and violin plots of selected lipid species in grey matter, including PI 38:4, PE 38:6, and PS 36:2, demonstrating significantly increased abundance in AD samples. **d**, Spatial distribution and quantification of representative lipids in white matter, including CL 72:8, PG 36:1, and PE O-36:4, confirming regionally enriched lipid alterations in AD. Statistical significance assessed via two-tailed t-tests; exact P-values indicated. (N>2000 pixels per 3 biological replicates)

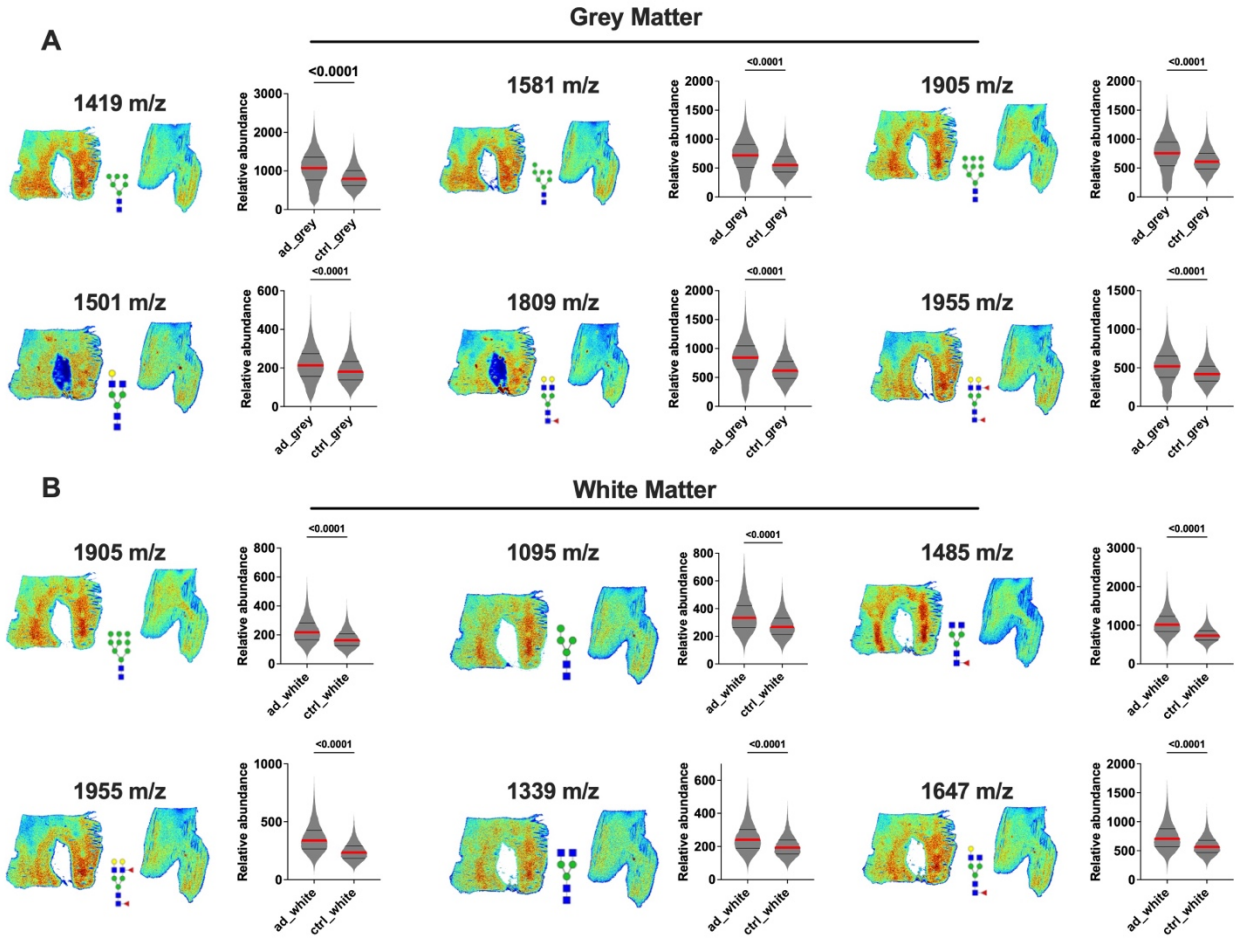

Supplementary Fig. 4 | Regional glycan abundance increases in human Alzheimer's disease brains. a, Spatial glycomics images and corresponding violin plots illustrating significantly elevated glycan abundance in grey matter regions of Alzheimer's disease (AD) brains relative to controls. Glycan species (1419, 1501, 1581, 1809, 1905, and 1955 m/z) exhibit consistent and significant increases in AD. Statistical analysis performed using two-tailed t-tests; exact P-values indicated. **b**, Spatial glycomics visualization and quantitative analysis of glycan abundance in white matter regions. Similar significant elevations observed across glycan species (1095, 1339, 1485, 1647, 1905, and 1955 m/z) in AD brains compared to controls (n>2000 pixels across three different samples). Statistical significance assessed by two-tailed t-tests; exact P-values indicated.

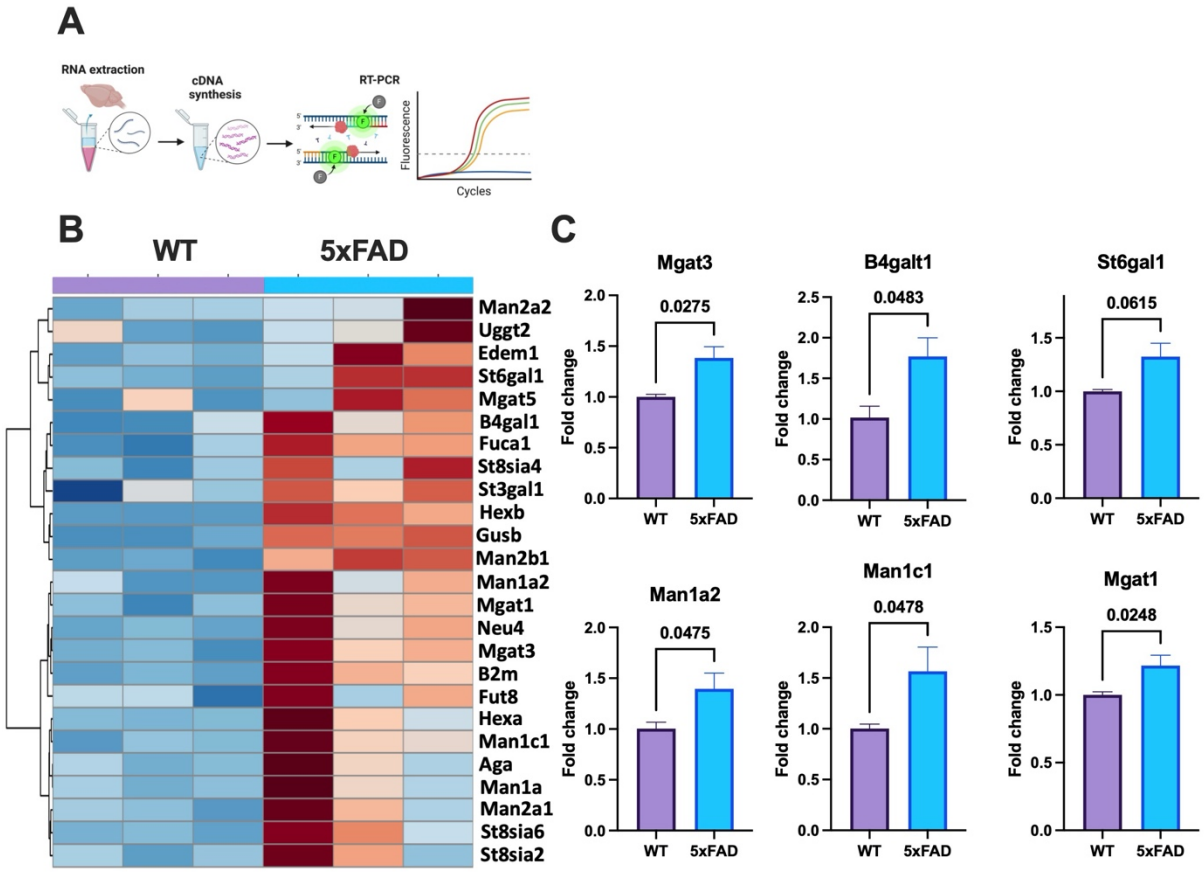

Supplementary Fig. 5 | Transcriptional upregulation of glycosylation-related genes in 5xFAD mouse brains. a, Schematic of experimental workflow for RNA extraction, cDNA synthesis, and RT-qPCR analysis of glycosylation-associated genes. **b**, Heatmap showing gene expression profiles of 27 glycosylation-related genes in wild-type (WT) and 5xFAD mouse brains. Hierarchical clustering reveals widespread transcriptional upregulation in 5xFAD mice. **c**, Bar graphs displaying fold change comparisons for selected glycosylation-related genes (Mgat3, B4galt1, St6gal1, Man1a2, Man1c1, and Mgat1) between WT and 5xFAD. Statistical significance determined by two-tailed t-tests; exact P-values indicated.

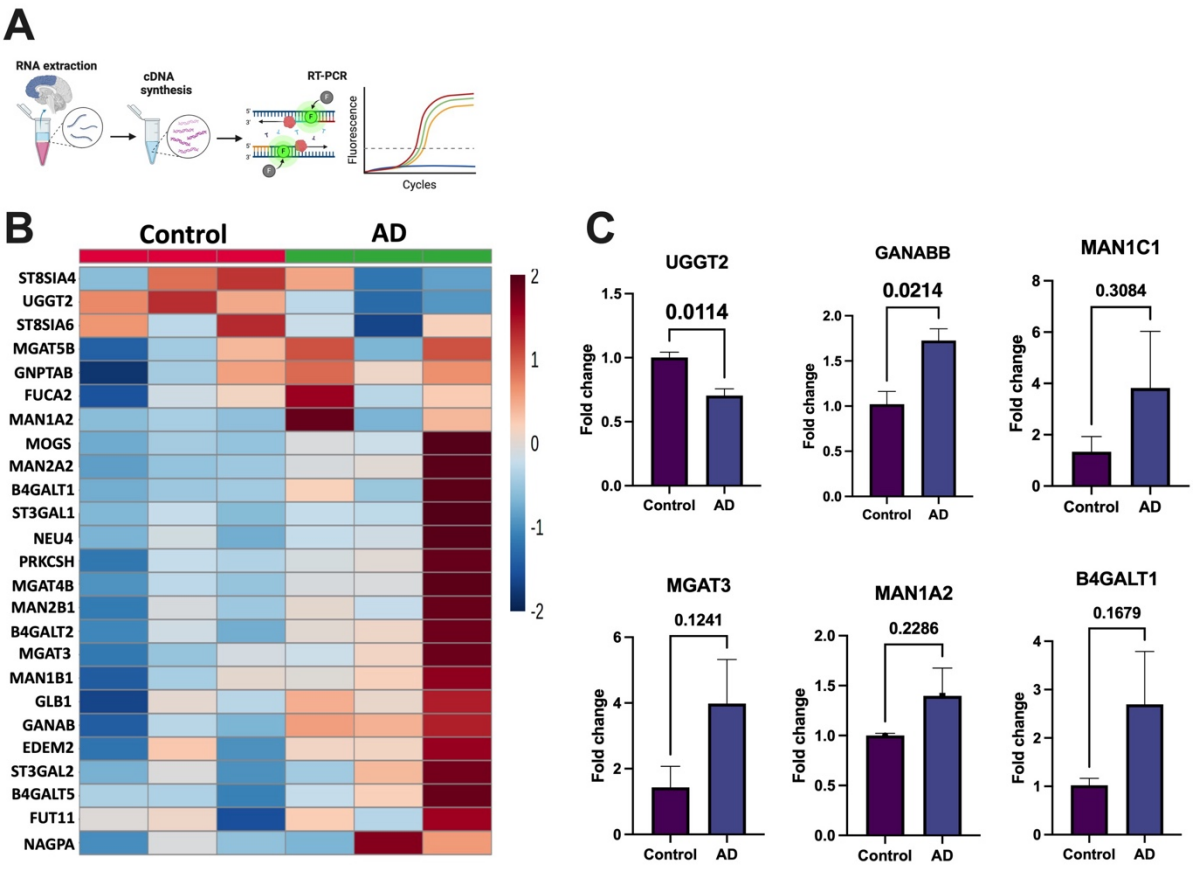

Supplementary Fig. 6 | Transcriptional profiling reveals altered expression of glycosylation-related genes in Alzheimer's disease human brain samples. a, Schematic of experimental workflow for RNA extraction, cDNA synthesis, and RT-qPCR used to quantify glycosylation gene expression in control and AD human brains. **b**, Heatmap showing hierarchical clustering of glycosylation-related gene expression across control and AD samples. Widespread dysregulation is observed, with several genes downregulated and others upregulated in AD. **c**, Bar plots showing fold change in expression for selected genes (UGGT2, GANAB, MAN1C1, MGAT3, MAN1A2, B4GALT1) with corresponding statistical comparisons. Two-tailed t-tests used; exact P-values indicated. (N=3 biological replicates)

A

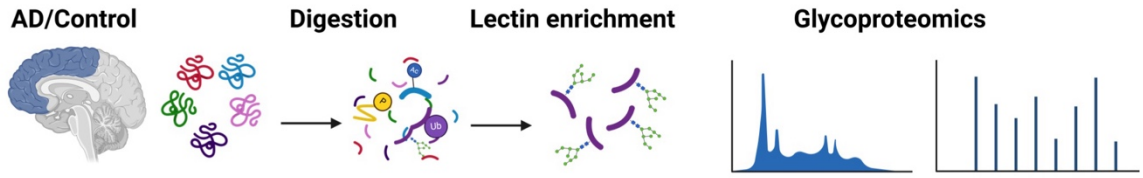
AD/Control
Digestion
Lectin enrichment
Glycoproteomics

B

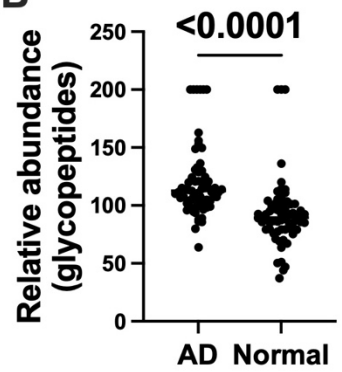
<0.0001
Relative abundance (glycopeptides)
250
200
150
100
50
0
AD
Normal

C

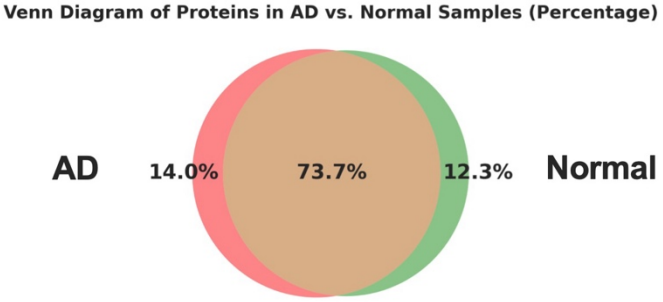
Venn Diagram of Proteins in AD vs. Normal Samples (Percentage)
AD
14.0%
73.7%
12.3%
Normal

D

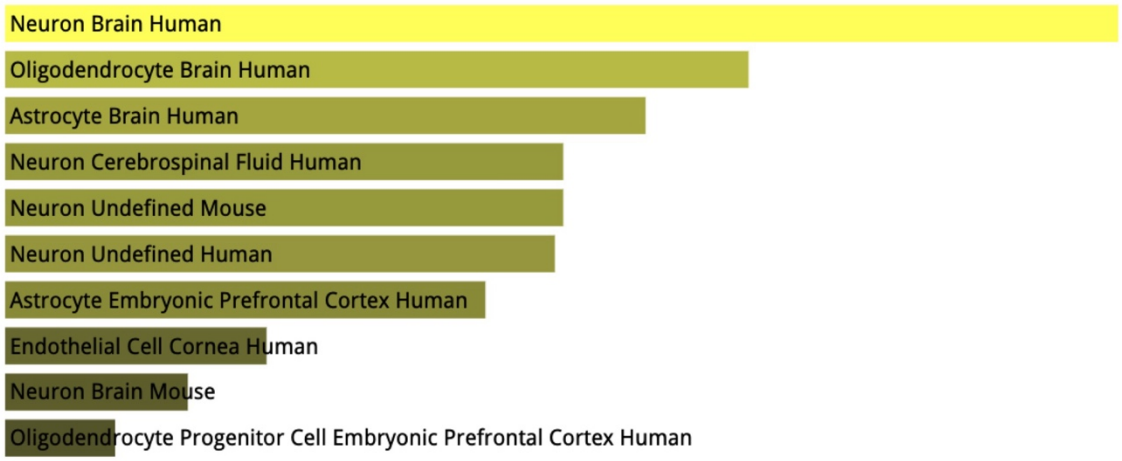
Neuron Brain Human
Oligodendrocyte Brain Human
Astrocyte Brain Human
Neuron Cerebrospinal Fluid Human
Neuron Undefined Mouse
Neuron Undefined Human
Astrocyte Embryonic Prefrontal Cortex Human
Endothelial Cell Cornea Human
Neuron Brain Mouse
Oligodendrocyte Progenitor Cell Embryonic Prefrontal Cortex Human

E

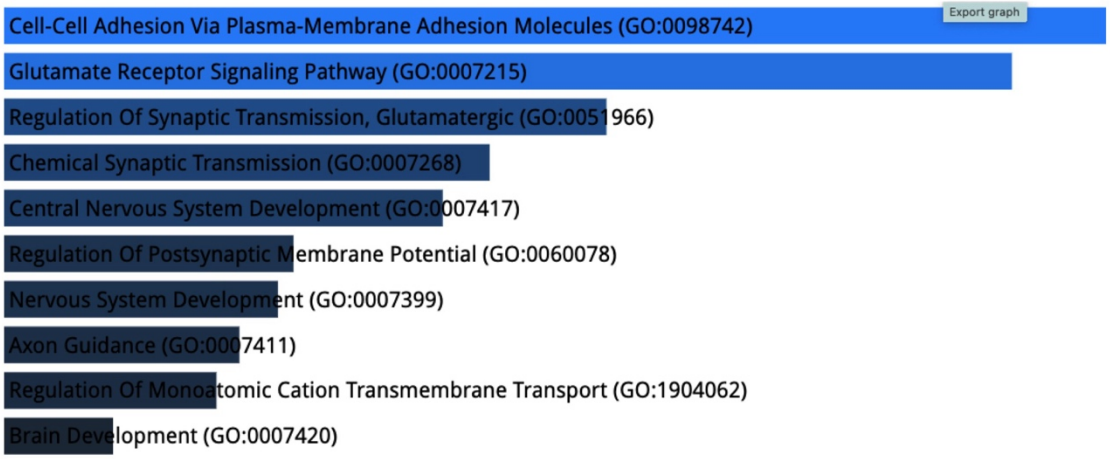
Export graph
Cell-Cell Adhesion Via Plasma-Membrane Adhesion Molecules (GO:0098742)
Glutamate Receptor Signaling Pathway (GO:0007215)
Regulation Of Synaptic Transmission, Glutamatergic (GO:0051966)
Chemical Synaptic Transmission (GO:0007268)
Central Nervous System Development (GO:0007417)
Regulation Of Postsynaptic Membrane Potential (GO:0060078)
Nervous System Development (GO:0007399)
Axon Guidance (GO:0007411)
Regulation Of Monoatomic Cation Transmembrane Transport (GO:1904062)
Brain Development (GO:0007420)

Supplementary Fig. 7| Glycoproteomic profiling reveals neuronal glycoprotein enrichment in Alzheimer's disease brains. a, Workflow depicting glycoproteomic analysis involving tissue homogenization, digestion, lectin-based glycopeptide enrichment, and mass spectrometry profiling from AD and control brain tissues. **b**, Quantification of total glycopeptide abundance reveals significantly elevated levels in AD samples compared to normal controls. Statistical analysis via two-tailed t-test.**c**, Venn diagram showing the overlap and distinct protein identities between AD and normal brain glycoproteomes. **d**, Cell type enrichment analysis indicates that glycoproteins upregulated in AD are predominantly expressed in neuronal and glial populations, including neurons, oligodendrocytes, and astrocytes. **e**, Gene ontology enrichment analysis reveals upregulated glycoproteins are significantly associated with neuronal functions including cell adhesion, synaptic signaling, and axon guidance.

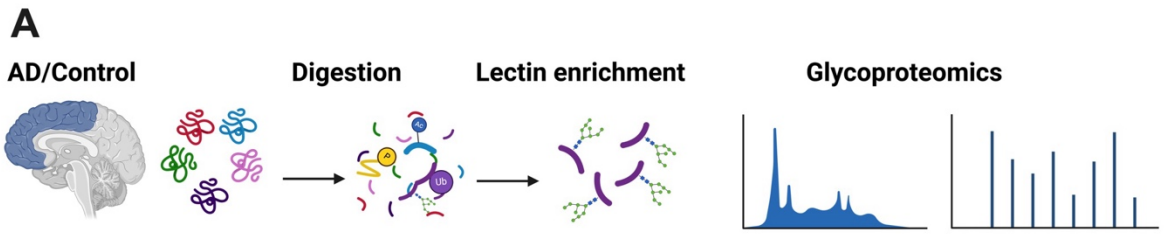
A
AD/Control
Digestion
Lectin enrichment
Glycoproteomics

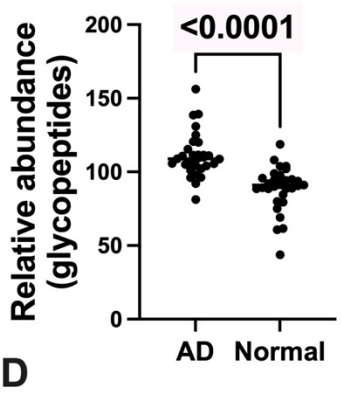
B
<0.0001
Relative abundance (glycopeptides)
200
150
100
50
0
AD
Normal

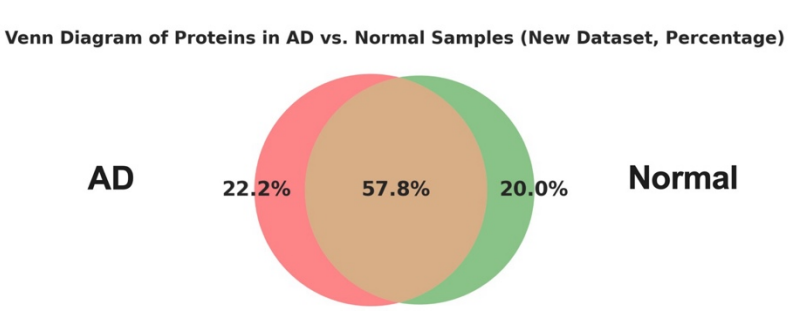
C
Venn Diagram of Proteins in AD vs. Normal Samples (New Dataset, Percentage)
AD
22.2%
57.8%
20.0%
Normal

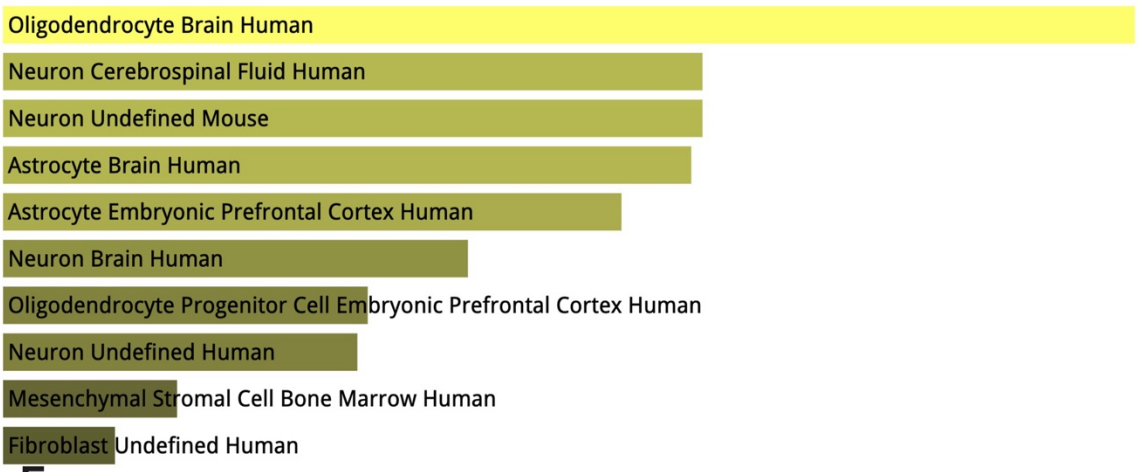
D
Oligodendrocyte Brain Human
Neuron Cerebrospinal Fluid Human
Neuron Undefined Mouse
Astrocyte Brain Human
Astrocyte Embryonic Prefrontal Cortex Human
Neuron Brain Human
Oligodendrocyte Progenitor Cell Embryonic Prefrontal Cortex Human
Neuron Undefined Human
Mesenchymal Stromal Cell Bone Marrow Human
Fibroblast Undefined Human

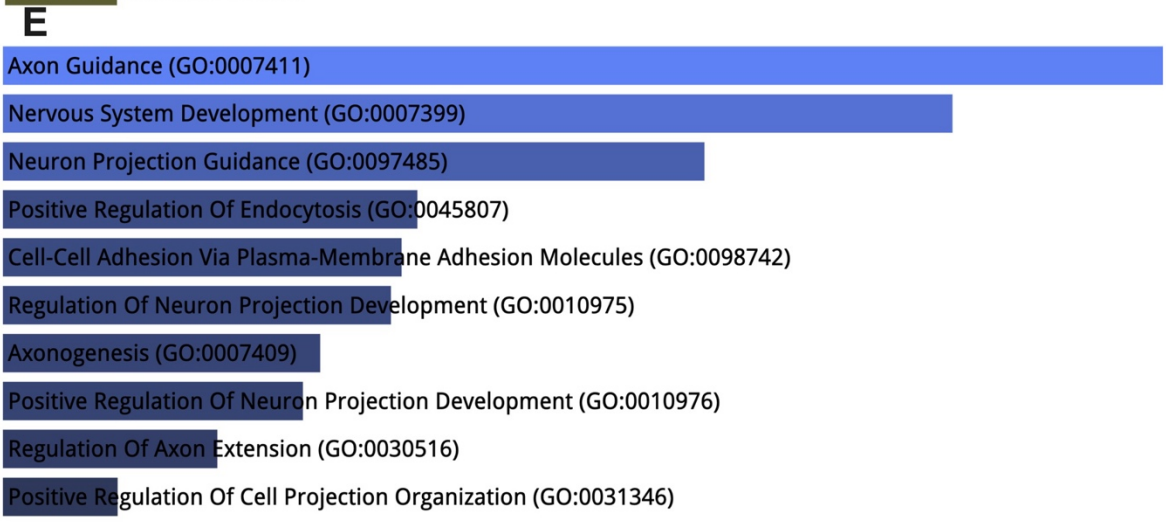
E
Axon Guidance (GO:0007411)
Nervous System Development (GO:0007399)
Neuron Projection Guidance (GO:0097485)
Positive Regulation Of Endocytosis (GO:0045807)
Cell-Cell Adhesion Via Plasma-Membrane Adhesion Molecules (GO:0098742)
Regulation Of Neuron Projection Development (GO:0010975)
Axonogenesis (GO:0007409)
Positive Regulation Of Neuron Projection Development (GO:0010976)
Regulation Of Axon Extension (GO:0030516)
Positive Regulation Of Cell Projection Organization (GO:0031346)

Supplementary Fig. 8 | Orthogonal glycoproteomic analysis confirms cell type–specific glycoprotein enrichment in human Alzheimer's disease. a, Experimental workflow showing sample preparation from AD and control human brains followed by protein digestion, lectin enrichment, and glycoproteomic mass spectrometry. **b**, Quantification of glycopeptide abundance reveals significantly elevated levels in human AD compared to control. Two-tailed t-test, ****P<0.0001. **c**, Venn diagram comparing protein identities across AD and control samples shows a higher proportion of unique glycoproteins in AD. **d**, Cell type enrichment analysis identifies oligodendrocytes and neurons as the major sources of AD-enriched glycoproteins. **e**, Gene ontology analysis reveals strong enrichment for axon guidance, nervous system development, and neuron projection–related pathways.

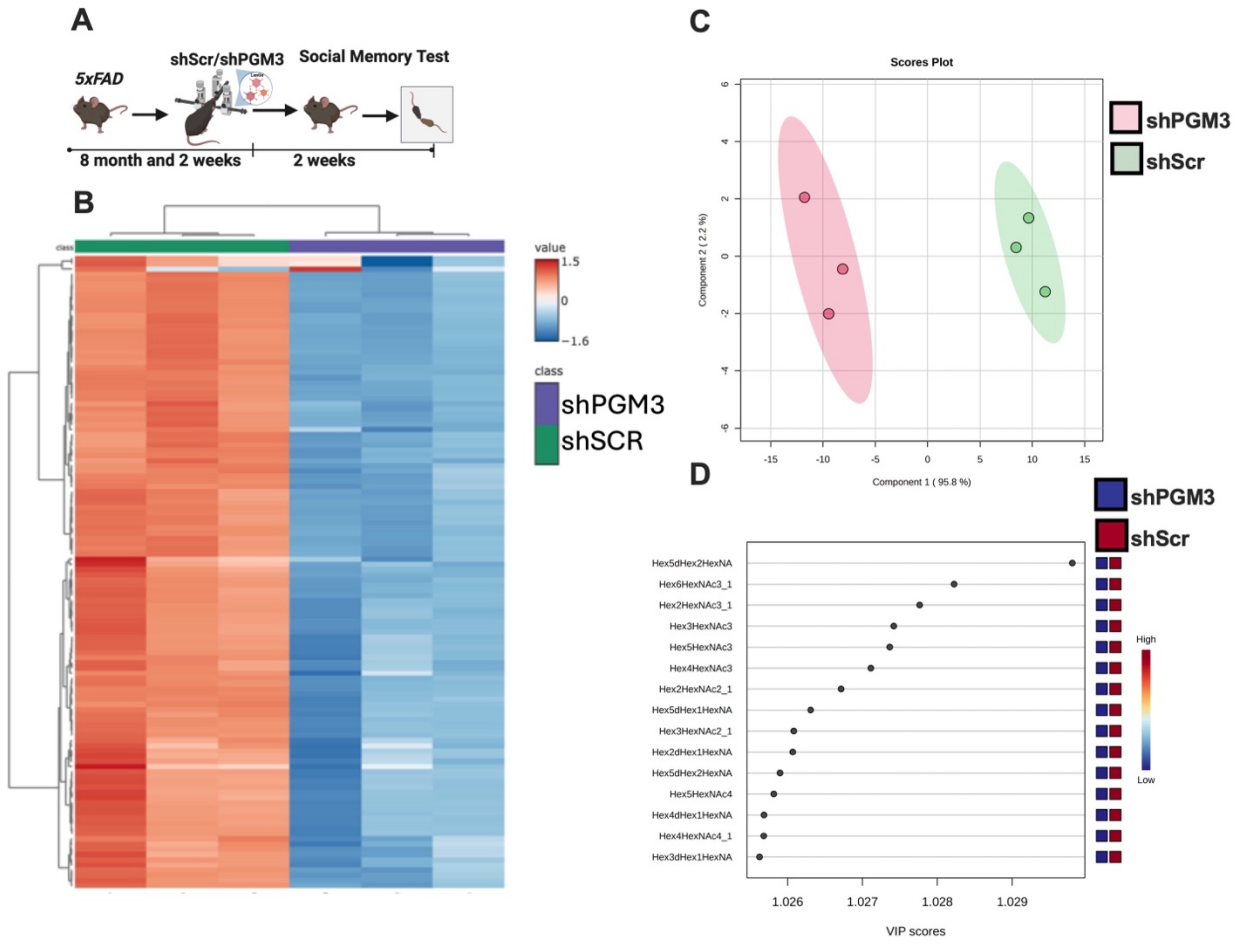

Supplementary Fig. 9 | PGM3 knockdown reshapes the brain N-glycan profile in 5xFAD mice. a, Experimental design: 8-month-old 5xFAD mice received ICV injections of shScr or shPGM3 and were analyzed 2 weeks later. **b,** Hierarchical clustering heat map of brain N-glycans showing a broad shift in glycan abundance between 5xFAD-shScr and 5xFAD-shPGM3 groups. **c**, Supervised multivariate scores plot (PLSDA) demonstrating clear separation of N-glycan profiles between shPGM3 and shScr mice. **d**, Variable importance in projection (VIP) plot highlighting the top N-glycan species that drive the separation, with most glycans decreased in shPGM3 brains.

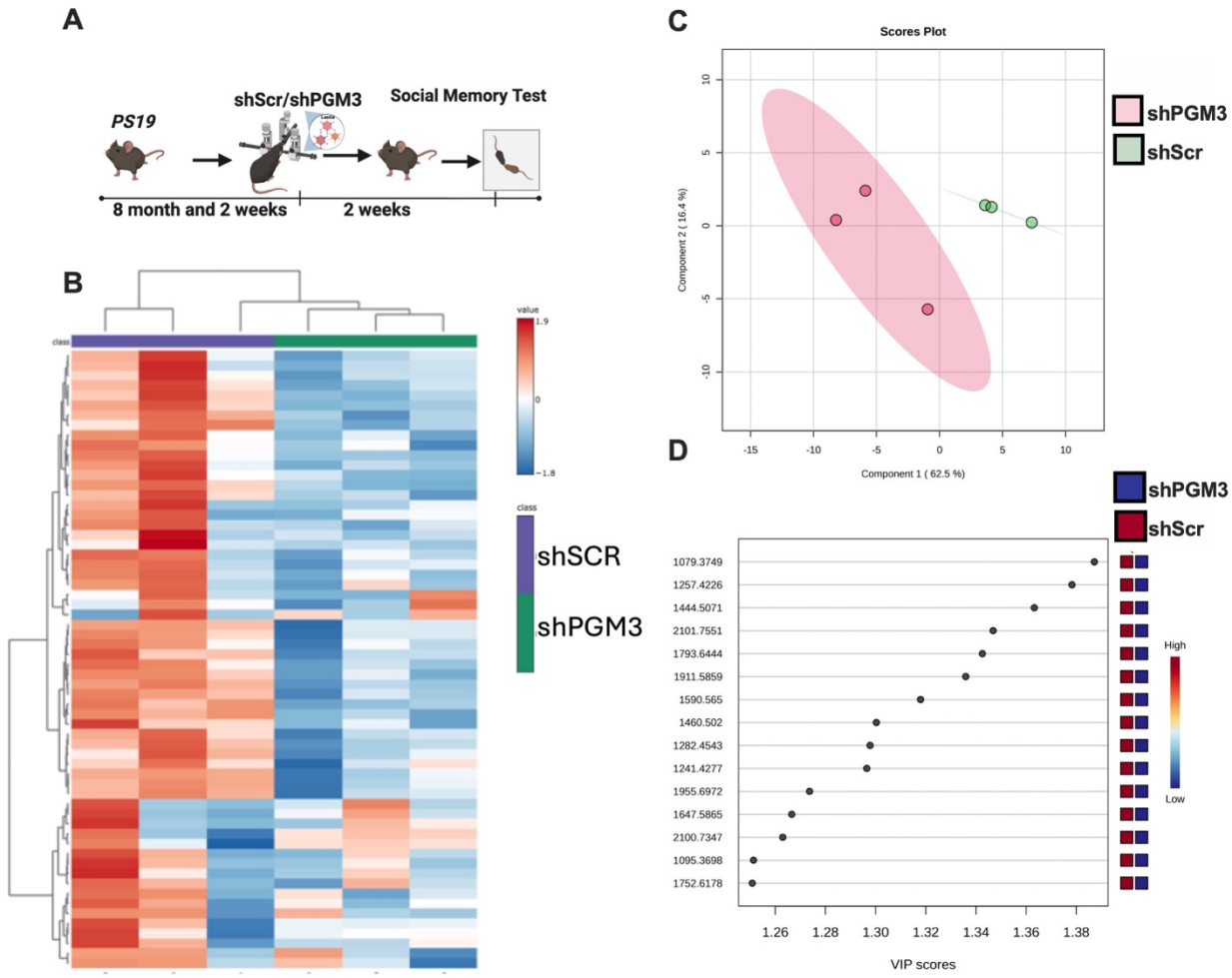

Supplementary Fig. 10 | PGM3 knockdown remodels the brain N-glycan landscape in PS19 mice. a, Experimental design: 8-month-old PS19 mice received ICV injections of shScr or shPGM3 and were analyzed 2 weeks later. **b**, Hierarchical clustering heat map of brain N-glycans showing a broad shift in glycan abundance between PS19-shScr and PS19-shPGM3 groups. **c,** Supervised multivariate scores plot demonstrating clear separation of N-glycan profiles between shPGM3 and shScr mice. **d**, Variable importance in projection (VIP) plot highlighting the top N-glycan m/z features driving this separation, with most glycans decreased in shPGM3 brains.

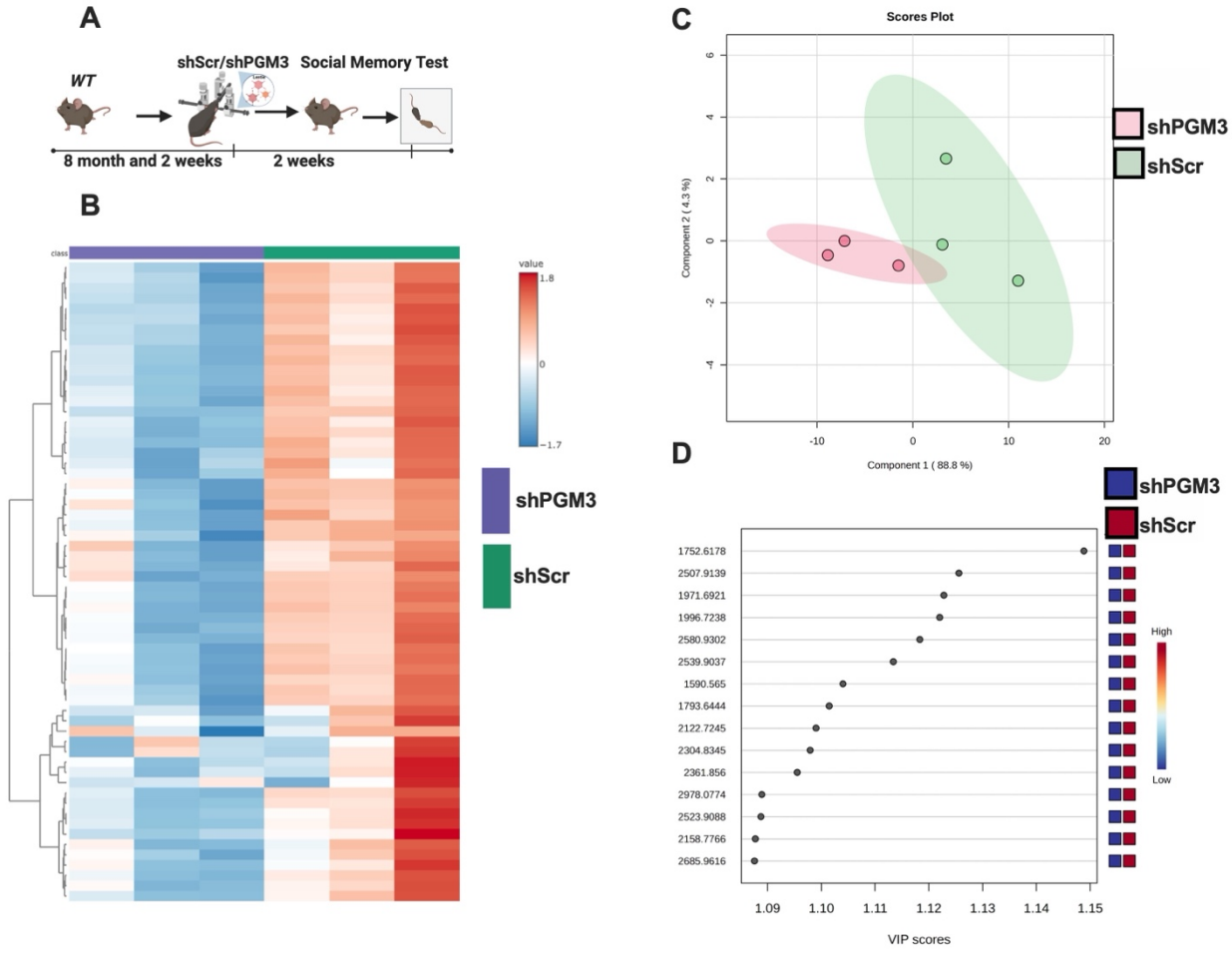

Supplementary Fig. **11** | PGM3 knockdown modestly alters the brain N-glycan profile in WT mice. **a**, Experimental design: 8-month-old WT mice received ICV injections of shScr or shPGM3 and were analyzed 2 weeks later. **b**, Hierarchical clustering heat map of brain N-glycans showing a shift in glycan abundance between WT-shScr and WT-shPGM3 groups.
c, Supervised scores plot demonstrating separation of N-glycan profiles between shPGM3 and shScr brains. **d**, Variable importance in projection (VIP) plot highlighting the top N-glycan m/z features contributing to this separation.

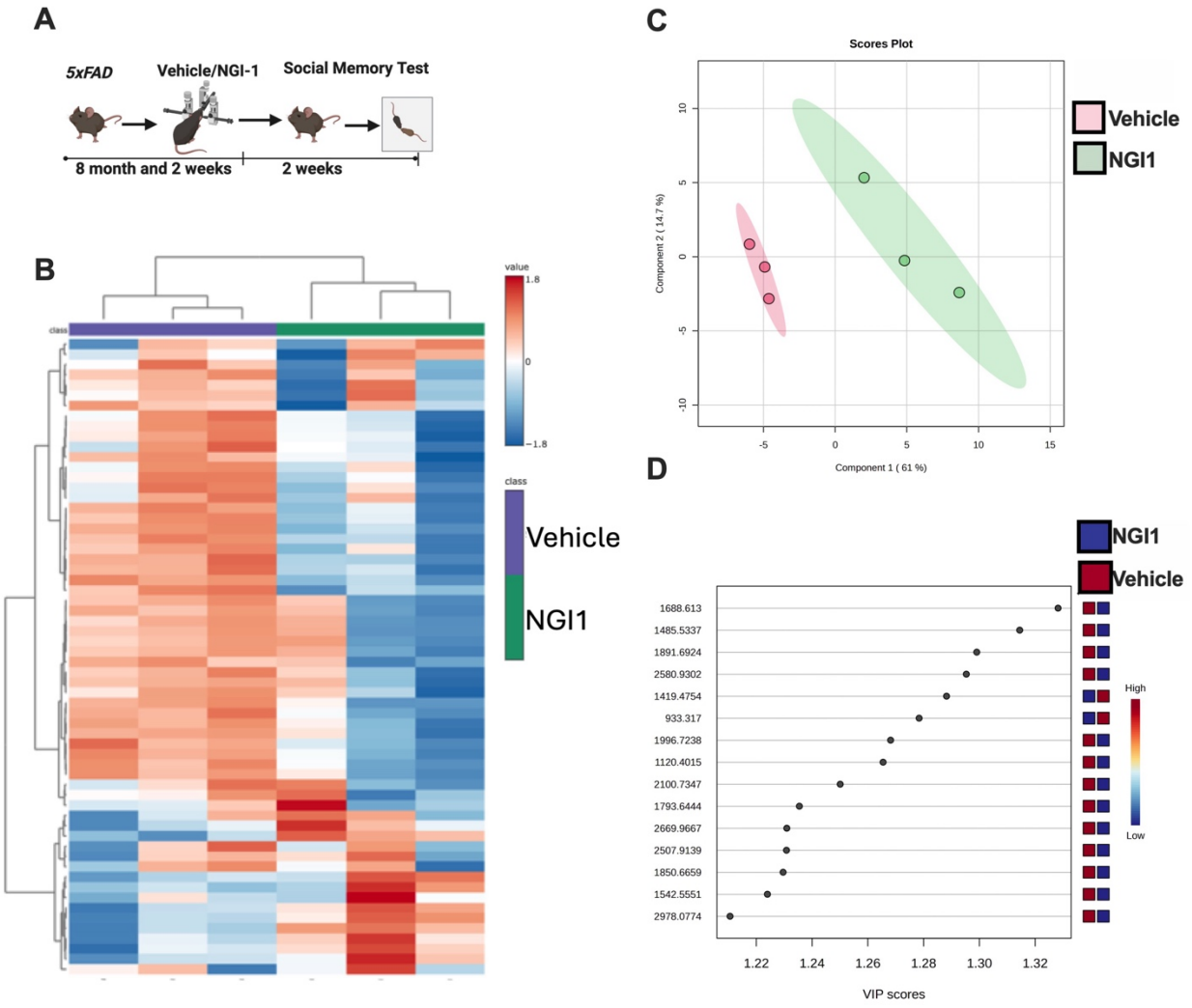

Supplementary Fig. 12| OST inhibition with NGI-1 remodels the brain N-glycan profile in 5xFAD mice. a, Experimental design: 8-month-old 5xFAD mice received intracerebral vehicle or NGI-1 and were analyzed 2 weeks later after social memory testing. **b**, Hierarchical clustering heat map of brain N-glycans showing a broad shift in glycan abundance between vehicle- and NGI-1–treated 5xFAD mice. **c**, Supervised multivariate scores plot demonstrating clear separation of N-glycan profiles in NGI-1 versus vehicle groups. **d**, Variable importance in projection (VIP) plot highlighting the top N-glycan m/z features that drive this separation, with most species decreased in NGI-1–treated brains.

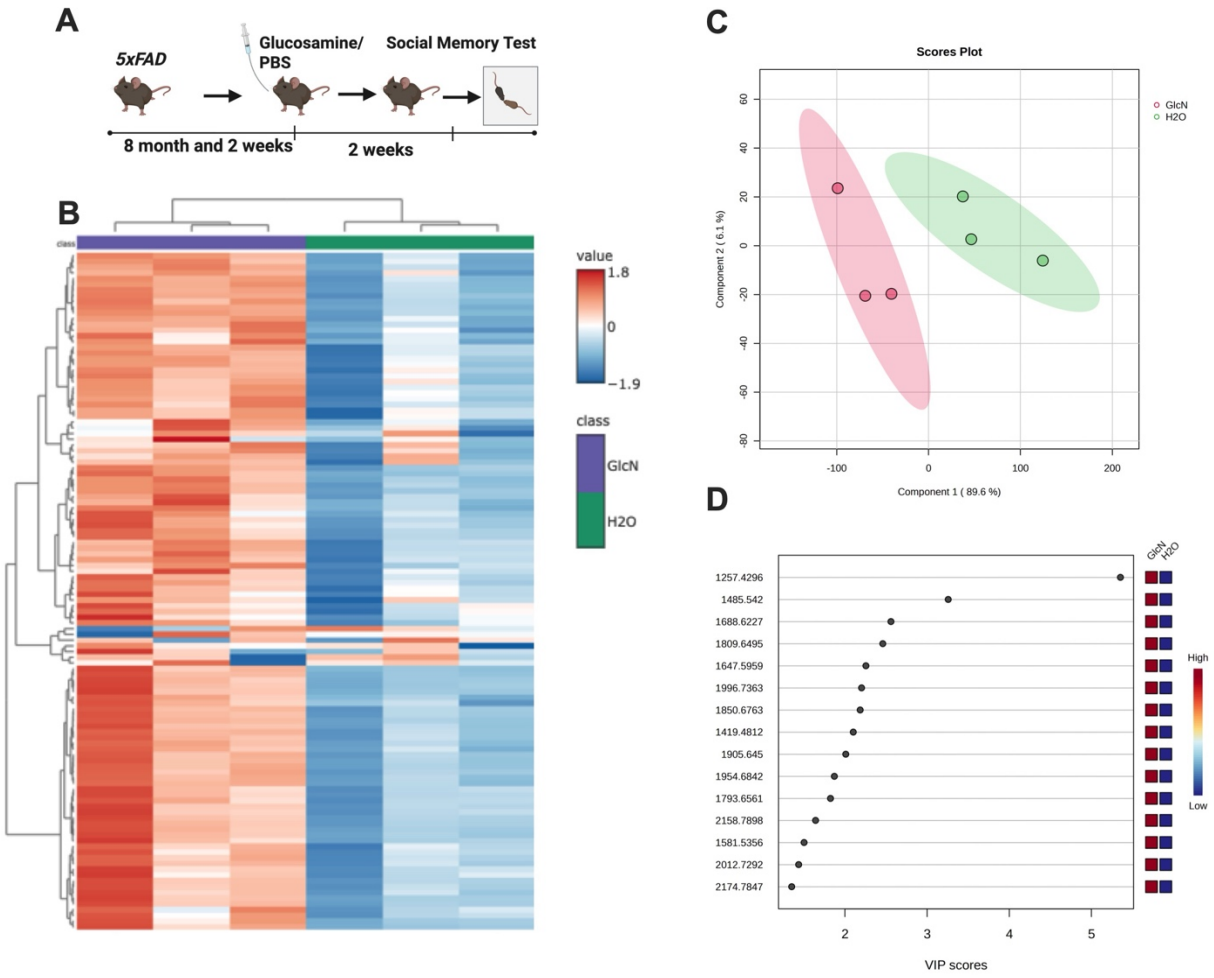

Supplementary Fig. 13| Glucosamine supplementation remodels the brain N-glycan profile in 5xFAD mice. a, Experimental design: 8-month-old 5xFAD mice received glucosamine or water (vehicle) for 2 weeks followed by social memory testing and brain collection. **b**, Hierarchical clustering heat map of brain N-glycans showing broad shifts in glycan abundance between glucosamine- and water-treated 5xFAD mice. **c**, Supervised multivariate scores plot demonstrating clear separation of N-glycan profiles in glucosamine versus water groups. **d**, Variable importance in projection (VIP) plot highlighting the N-glycan m/z features that most strongly discriminate glucosamine-treated from water-treated brains.

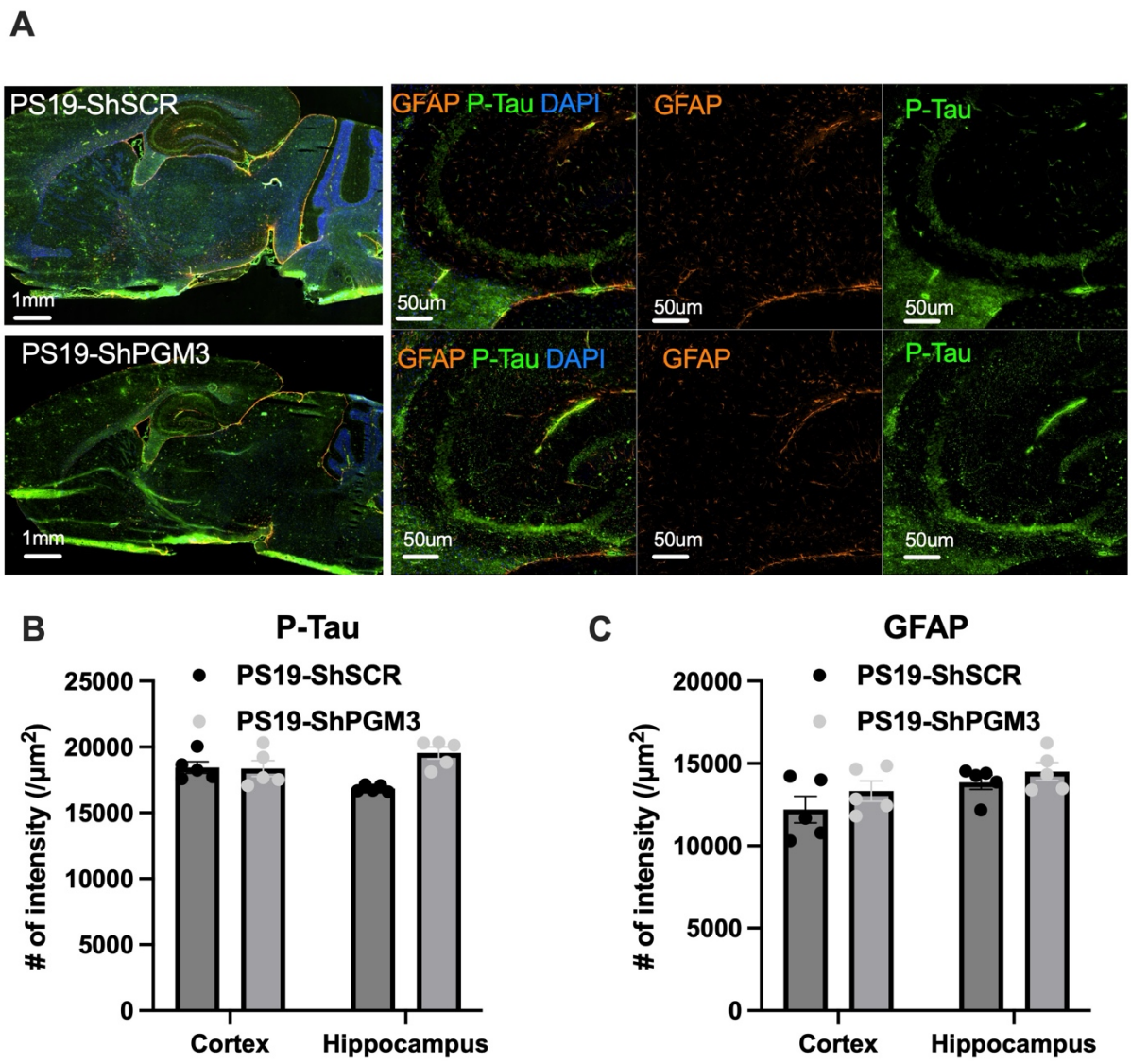

Supplementary Fig. 14| PGM3 knockdown does not alter tau pathology or astrocytosis in PS19 mice. a, Immunofluorescence images of phospho-tau (P-tau) and GFAP in cortex and hippocampus from PS19-shScr and PS19-shPGM3 mice. **b,** Quantification of P-tau signal intensity in cortex and hippocampus showing comparable levels between PS19-shScr and PS19-shPGM3 groups. **c,** Quantification of GFAP intensity in cortex and hippocampus indicating unchanged astrocytic activation after PGM3 knockdown. Data are mean ± s.e.m.; two-tailed t-test; ns, not significant.

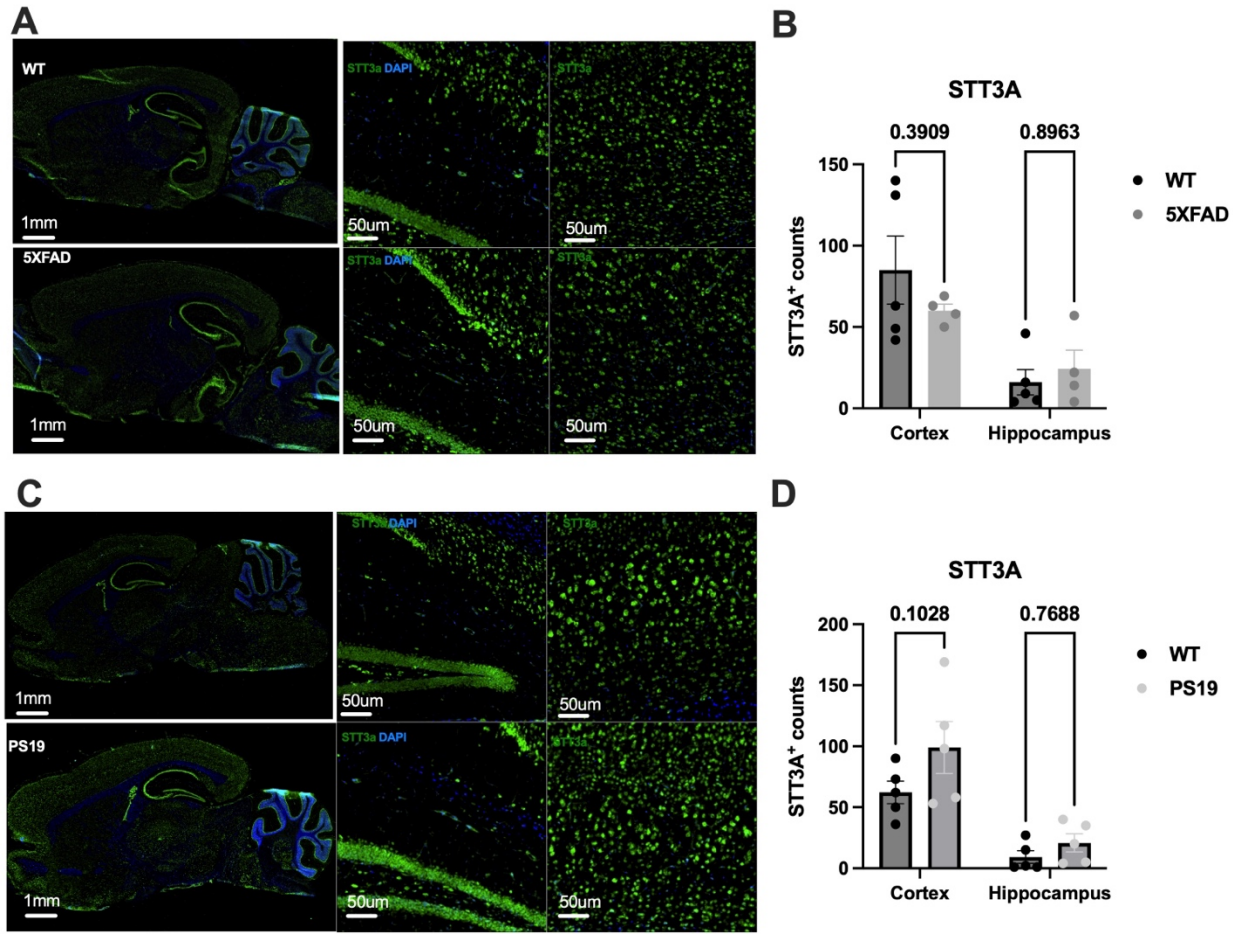

Supplementary Fig. 15 | STT3A expression is unchanged in 5xFAD and PS19 mouse brains. **a**, Immunofluorescence staining of STT3A in cortex and hippocampus of WT and 5xFAD mice. **b**, Quantification of STT3A$^+$ cells in cortex and hippocampus showing no significant difference between WT and 5xFAD mice. **c,** STT3A staining in cortex and hippocampus of WT and PS19 mice. **d**, Quantification of STT3A$^+$ cells indicating comparable expression between WT and PS19 mice. Data are mean ± s.e.m.; P values are indicated (two-tailed t-test); ns, not significant.

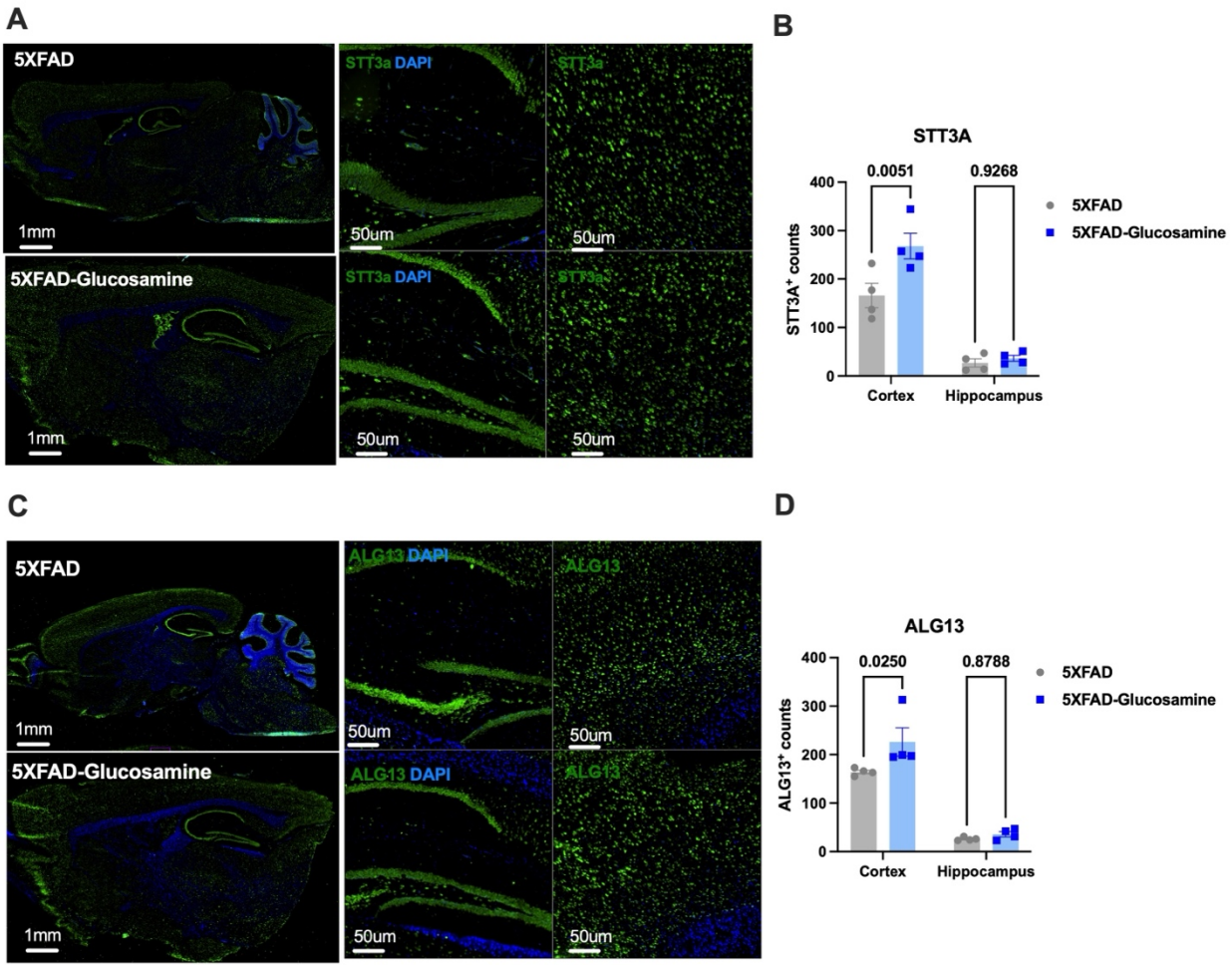

Supplementary Fig. 16 | Glucosamine modestly increases cortical LLO biosynthesis enzymes in 5xFAD mice. a, Immunofluorescence staining of STT3A in cortex and hippocampus of 5xFAD mice treated with water or glucosamine. **b**, Quantification of $STT3A^+$ cells shows a modest increase in cortex but no change in hippocampus of glucosamine-treated 5xFAD mice compared with water-treated controls. **c**, ALG13 staining in cortex and hippocampus of water- and glucosamine-treated 5xFAD mice.**d,** Quantification of $ALG13^+$ cells reveals increased cortical ALG13 with glucosamine and no significant difference in hippocampus.
Data are mean ± s.e.m.; P values are indicated (two-tailed t-test); ns, not significant.

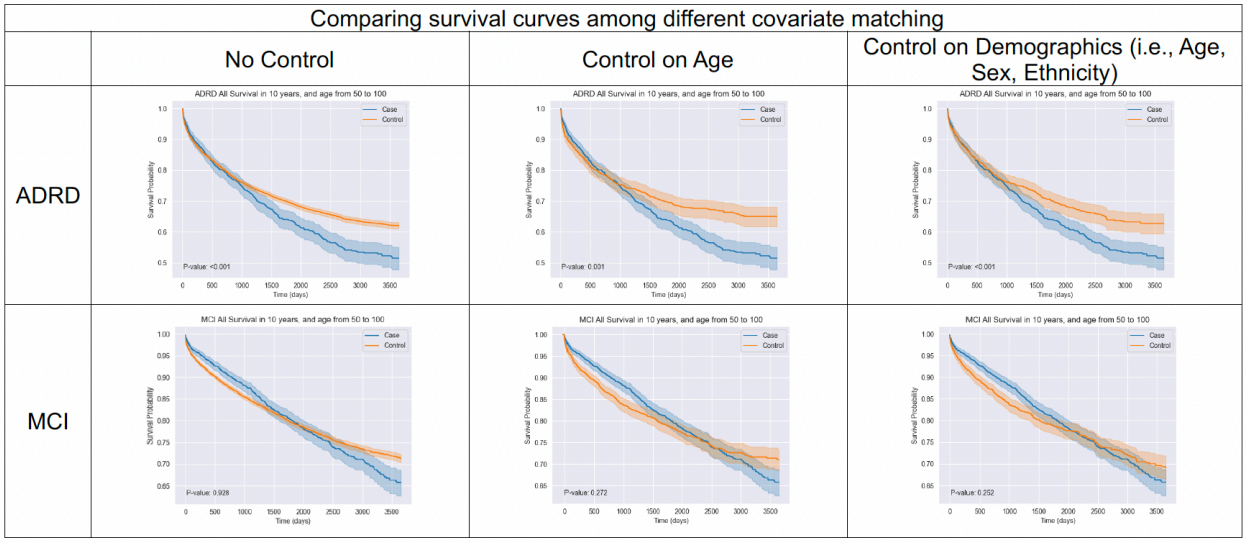

Supplementary Fig. 17 | Survival in ADRD and MCI patients with or without glucosamine use under different covariate matching strategies. Kaplan–Meier curves show 10-year all-cause survival in glucosamine users (case) and non-users (control) for ADRD (top row) and MCI (bottom row) under three conditions: no covariate control (left), age-matched (middle) and age plus demographic (age, sex, ethnicity) matched (right). Shaded areas indicate 95% confidence intervals, and log-rank P values for case versus control are shown in each panel.

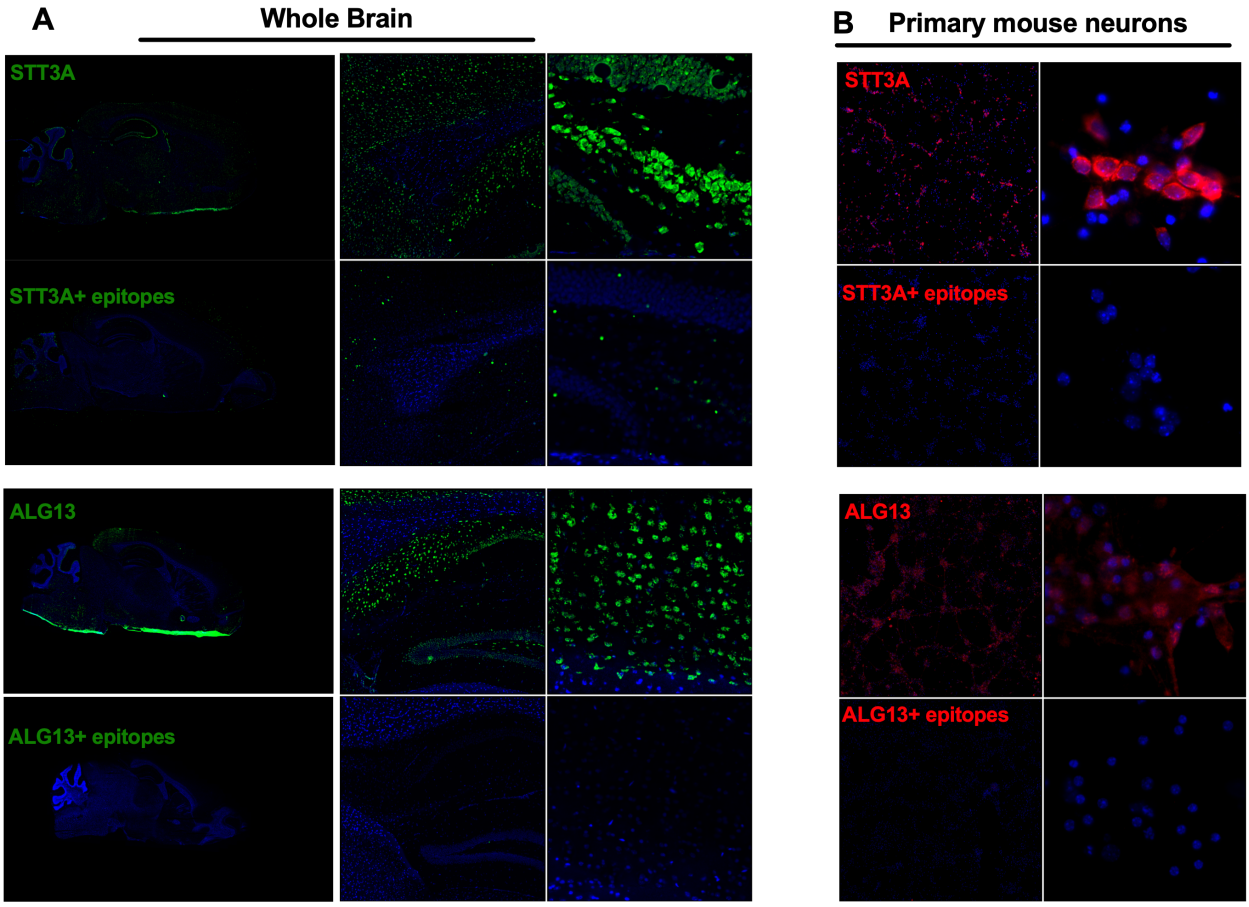

Supplementary Fig. 18 | Epitope competition validates STT3A and ALG13 antibody specificity in whole brain sections and primary mouse neurons. a, Immunofluorescence staining of STT3A and ALG13 in whole brain sections shows clear signal under standard primary antibody conditions, whereas co-incubation with the corresponding blocking epitope markedly reduces signal. For each target, images are shown at low magnification for the whole section, followed by higher-magnification regional views. **b,** Immunofluorescence staining of STT3A and ALG13 in primary mouse neurons shows robust cellular labeling that is strongly reduced or abolished by co-incubation with the corresponding blocking epitope. Nuclei are counterstained with DAPI (blue) for both a and b.